Chapter 4
Mathematical Model and Prototype of Fish-Swimming Motion in a Wheeled Robotic Platform

E. S. Calderón, N. E. Carusetta, M. R. Deverell, J. D. Blessinger, M. J. Ward, J. Ardister, and B. F. Feeny

Abstract Mimicking oscillatory fish swimming dynamics on land platforms, such as autonomous vehicles or domestic robots, can enable more efficient movement. This project explores the development of a "landfish" robot: a wheeled platform that produces fish-like motion on a flat, dry surface through oscillatory motion of the tail relative to the head. A reduced-order model of fish swimming dynamics, which simplifies the fin-water interaction, has been developed in previous work [1]. In this study, a reduced-order model based on nonholonomic constraints in carangiform swimming will be developed and used to inform hardware changes for a wheeled robotic platform. We will then operate the landfish at a range of modulating tail frequencies and amplitudes, measure and characterize the steady-state dynamic response, and compare experimental results with simulations from the reduced-order model.

Keywords Biomimetic robots · Carangiform swimming · Nonholonomic constraints · Fish-inspired locomotion · Reduced-order modeling

Introduction

While human ingenuity has developed machines that excel at their tasks on paved roads or charted waters, these designs are limited in their performance when exposed to unique and difficult environments. By contrast, animals have developed exceptional abilities to survive in inhospitable or niche habitats around the world. These observations have led to a growing field of bio-inspired robots, which are better suited to performing in natural environments compared to their traditional robotic counterparts.

Fish, the most diverse group of vertebrates, are a popular source of inspiration for these designs [2]. Bio-inspired fish robots (e.g. [3], [4], and [5]) have the advantages of high efficiency, advanced maneuverability, low noise emission, and autonomous control capabilities. Beyond the creation of more efficient machines, robot development has additionally allowed scientists to model animal behavior in controlled environments [6]. Understanding how animals move and interact with their surroundings is critical to improving pre-existing engineering designs of underwater and hybrid terrain vehicles and developing new insights about the natural world.

E. S. Calderón
Departments of Mathematics and Physics, Whitworth University, Spokane, WA 99251
e-mail: ecalderon27@my.whitworth.edu

N. E. Carusetta · M. R. Deverell
Department of Mechanical Engineering, Rice University, Houston, TX 77005
e-mail: ec65@rice.edu; matthewrdeverell@gmail.com

J. D. Blessinger · M. J. Ward
Los Alamos National Laboratory, Los Alamos, NM 87545
e-mail: jbless@lanl.gov; mjward@lanl.gov

J. Ardister · B. F. Feeny
Department of Mechanical Engineering, Michigan State University, East Lansing, MI 48824
e-mail: ardiste3@msu.edu; feeny@egr.msu.edu

Kristin B. Zimmerman, PhD (eds.), *Structural Health Monitoring, Metamaterials, Metastructures and Additive Manufacturing and Dynamics of Biomedical and Bioinspired Systems, 2026, Vol. 10*, Conference Proceedings of the Society for Experimental Mechanics Series, https://doi.org/10.1007/978-8-743-81449-8_4

While there are several common undulatory swimming motions, carangiform [7, 8, 9] is especially popular to research for its balanced high speed and maneuverability. In carangiform motion, the anterior section of the body is stiff relative to the posterior; the last third undulates rapidly to produce propulsion [10]. At sufficiently high Strouhal numbers ($St > 0.22$), the wave speed of the fish exceeds its forward swimming speed, thereby accelerating the flow at the posterior region of the body and preventing flow separation from occurring, which significantly reduces drag [11]. Due to this increased efficiency, as well as an overall balance between speed and maneuverability, carangiform motion has been robustly explored over the past two decades, with notable research including biomimetic tuna [12], wire-driven flapping propulsors [13], and flexible caudal fins [14].

Our work endeavors to explore the movement of carangiform swimming by approximating a fish's motion using nonholonomic constraints imposed by its fins cutting through water [15, 16, 17, 18, 19, 1]. Through exploring the motion of a "landfish" with similar constraints imposed by wheels without slipping, we aim to better understand the motion of fish without the added fluid dynamic complexities like unsteady flow effects or vortex shedding. This research builds on previous Chaplygin sleigh designs that used casters on some wheels instead of nonholonomic constraints on all wheels [20]. While our design cannot perfectly describe the motion of a fish in water due to the lack of continuous body deformation, fluid deformation, and other simplifying assumptions, this research establishes a critical benchmark against which more complex "finned" models can be compared and validated, and can pave the way for faster optimization workflows for future biomimetic robots.

This paper presents a reduced-order model of fish-inspired locomotion, beginning with a mathematical formulation using three distinct approaches, followed by the experimental implementation of a wheeled landfish prototype, comparison of simulation and experimental results across varying tail oscillation parameters, and concluding with insights on the efficacy of our approach for modeling biomimetic locomotion. By eliminating the complexities of fluid dynamics, we can more easily develop and analyze a computationally inexpensive reduced-order model that still captures the essential dynamics of carangiform swimming.

Methodology

Mathematical Model

We used three different mathematical approaches for deriving equations of motion: Lagrange multipliers, nonholonomic Lagrange, and the principle of virtual power. These are common methods for solving nonholonomically-constrained systems [21, 22]. For all three methods, q_k represents a generalized coordinate. After implementing the holonomic constraints, our system has three generalized coordinates to keep track of: x, y, and θ. These will also be referred to as q_x, q_y, and q_θ. A superscript of u or c signifies that the quantity is nonholonomically unconstrained or constrained, respectively.

Figure 1 shows a diagram of the landfish system, which comprises two rigid bodies: the head and the tail. The head position is denoted by coordinates $x_1 = x$, $y_1 = y$, while the tail position is represented by x_2, y_2. The angle θ defines the

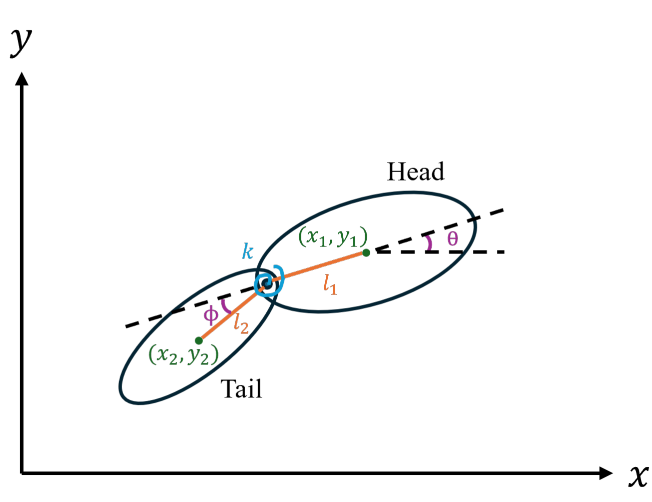

Fig. 1 System diagram of the landfish model showing the two-body configuration with the head and tail, from which the equations of motion for our mathematical model are derived

head's rotation relative to the horizontal x axis, while ϕ represents the tail's rotation relative to the head, which is imposed independently as

$$\phi = a\sin(\omega t + \beta). \tag{1}$$

Table 1 provides definitions for these parameters which include body components and physical coefficients. All parameters are referenced from the center of mass of their respective body.

Table 1 Physical and kinematic parameters of the landfish model

Parameter of Interest	Definition	Units
(x_1, y_1)	Cartesian position of head	m
(x_2, y_2)	Cartesian position of tail	m
θ	Rotational angle of head	deg
ϕ	Rotational angle of tail	deg
a	Amplitude of ϕ	rad
ω	Frequency of ϕ	$\frac{\text{rad}}{\text{s}}$
l_1	Length from head to joint	m
l_2	Length from tail to joint	m
m_1	Mass of head	kg
m_2	Mass of tail	kg
I_1	Moment of inertia of head	kg·m^2
I_2	Moment of inertia of tail	kg·m^2
k	Torsional stiffness	$\frac{\text{N}}{\text{rad}}$
C_d	Quadratic drag coefficient	$\frac{\text{kg}}{\text{m}}$
μ_k	Coulomb friction coefficient	[-]

Applying three holonomic contraints and two nonholonomic contraints to x_1, y_1, x_2, y_2, θ, and ϕ reduces our six coordinates to a single degree of freedom system ($n = 1$). This process is described below. Because we are controlling the motion of the tail, there is a constraint on ϕ as seen in Equation 1. There are also two holonomic constraints associated with describing the position of the tail with respect to that of the head through trigonometry. Thus, the position vectors for the head and tail, respectively, can be written in terms of x, y, θ, and ϕ, as

$$\vec{r}_1^{\,u} = \begin{bmatrix} x_1 \\ y_1 \end{bmatrix} = \begin{bmatrix} x \\ y \end{bmatrix} \tag{2a}$$

$$\vec{r}_2^{\,u} = \begin{bmatrix} x_2 \\ y_2 \end{bmatrix} = \begin{bmatrix} x - l_1\cos(\theta) - l_2\cos(\theta+\phi) \\ y - l_1\sin(\theta) - l_2\sin(\theta+\phi) \end{bmatrix}. \tag{2b}$$

The velocity of each body acts along its respective orientation, creating nonholonomic constraints that can be written as

$$\dot{y}_1 = \dot{x}_1\tan(\theta) \tag{3a}$$

$$\dot{y}_2 = \dot{x}_2\tan(\theta+\phi), \tag{3b}$$

which can be cast in Pfaffian (differential) form, or solved for $\dot{\theta}$ and y, generally as

$$a_{jx}dx + a_{jy}dy + a_{j\theta}d\theta + a_{j\phi}d\phi = 0 \qquad \text{for } j = 1, 2 \tag{4a}$$

$$\dot{\theta} = \alpha_{\theta x}\dot{x} + \alpha_{\theta\phi}\dot{\phi} \tag{4b}$$

$$\dot{y} = \alpha_{yx}\dot{x} + \alpha_{y\phi}\dot{\phi}. \tag{4c}$$

Note that Equations (4c) and (3a) match given $\dot{y}_1 = \dot{y}$ and $\dot{x}_1 = \dot{x}$. Implementing these constraints to solve for $\dot{\theta}$ results in

$$\dot{\theta} = \frac{-l_2\dot{\phi} - \dot{x}\sin(\phi)\sec(\theta)}{l_1\cos(\phi) + l_2}. \tag{5}$$

Because our system has a single degree of freedom, we can define an independent coordinate, x, and constrained coordinates, y and θ (whose time derivatives are defined in Equations (3a) and (5)).

Two of the employed methods, Lagrange multipliers and nonholonomic Lagrange, are based on Euler-Lagrangian mechanics and thus use the unconstrained Lagrangian,

$$L^u = T^u - V, \tag{6}$$

where the kinetic energy, T^u, and potential energy, V, are defined as

$$T^u = \frac{1}{2}m_1(\dot{x}_1^2 + \dot{y}_1^2) + \frac{1}{2}m_2(\dot{x}_2^2 + \dot{y}_2^2) + \frac{1}{2}I_1\dot{\theta}^2 + \frac{1}{2}I_2(\dot{\theta} + \dot{\phi})^2$$

$$V = -\frac{1}{2}k_1\theta^2 - \frac{1}{2}k_2\phi^2.$$

The only losses accounted for in our system are Coulomb friction and air drag in the Cartesian plane. For all three methods, we define these forces as

$$\vec{F^u} = \begin{bmatrix} -g\sin(\theta)(C_d(\dot{y}^2 + \dot{x}^2) + \mu_k(m_1 + m_2)) \\ -g\cos(\theta)(C_d(\dot{y}^2 + \dot{x}^2) + \mu_k(m_1 + m_2)) \end{bmatrix}. \tag{7}$$

The **Lagrange multipliers (LM)** method uses

$$\frac{d}{dt}\frac{\partial L^u}{\partial \dot{q_k}} - \frac{\partial L^u}{\partial q_k} = Q_k + \sum_{j=1}^{p} a_{jk}\lambda_j, \tag{8}$$

where λ_j are introduced as Lagrange multipliers, which in this case represent the magnitude of the generalized force needed to enforce the nonholonomic constraints present in our system. For LM, because there are two nonholonomic constraints ($p = 2$) and one degree of freedom, there are three k indices, which correspond to x, y, and θ. The a_{jk}-values come from the Pfaffian form shown in Equation (4a).

Given that ϕ is an imposed parameter rather than a generalized parameter, the $a_{j\phi}$ coefficient is not included in the constraint formulation. The non-conservative force term, Q_k, is defined as

$$Q_k = \vec{F^u} \cdot \frac{\partial \vec{r}^u}{\partial q_k} + \vec{M} \cdot \frac{\partial \vec{\omega}^u}{\partial \dot{q_k}}, \tag{9}$$

where $\vec{M}$ represents the external moments on the head and tail. Consequently, the generalized forces Q_x and Q_y are equivalent to the corresponding components of $\vec{F^u}$.

The **nonholonomic Lagrange (NHL)** method [21] applies

$$\frac{d}{dt}\frac{\partial L^u}{\partial \dot{q_k}} - \frac{\partial L^u}{\partial q_k} + c_k = Q_k \tag{10}$$

where, because we choose x to be our independent coordinate, $k = x$ and we define

$$c_k = \left(\frac{d}{dt}\frac{\partial L^u}{\partial \dot{y}} - \frac{\partial L^u}{\partial y}\right)\alpha_{xy} + \left(\frac{d}{dt}\frac{\partial L^u}{\partial \dot{\theta}} - \frac{\partial L^u}{\partial \theta}\right)\alpha_{x\theta}.$$

Similar to LM, $p = 2$ continues to represent the number of nonholonomic constraints. The two α-terms are defined in Equations (4b, 4c). They result from solving the nonholonomic constraint Equations (3a, 3b) for our two dependent velocities, $\dot{y}$ and $\dot{\theta}$, only in terms of our independent velocity, $\dot{x}$. The losses term, Q_k, is defined as

$$Q_k = \vec{F^c} \cdot \frac{\partial \dot{\vec{r}^c}}{\partial \dot{q_k}} + \vec{M} \cdot \frac{\partial \vec{\omega}^c}{\partial \dot{q_k}}, \tag{11}$$

where constrained derivatives of $\vec{r}_1$ in Equation (2a), and the friction force defined in Equation (7) on the head, define $\dot{\vec{r}^c}$ and $\vec{F^c}$. Note that, beyond the constraint equations, there is only one equation and thus one Q_k term.

The **principle of virtual power (PVP)** method is defined by [22],

$$\sum_{j=1}^{N} m_i \ddot{\vec{r}}_i \cdot \frac{\partial \dot{\vec{r}}_i^c}{\partial \dot{q}_k} + \sum_{j=1}^{N} I_i \ddot{\theta}_i \frac{\partial \omega^c}{\partial q_k} = Q_k, \tag{12}$$

where $N = 2$ is the number of bodies, k indexes the independent coordinates (only x in this case), and θ_i is the angular displacement of body i with respect to the inertial frame. That is, $\theta_1 = \theta$, and $\theta_2 = \theta + \phi$. Thus Equation (12) can also be written as

$$\sum_{j=1}^{N} m_i \ddot{\vec{r}}_i \cdot \frac{\partial \dot{\vec{r}}_i^c}{\partial \dot{q}_k} + I_1 \ddot{\theta} \alpha_{x\theta} + I_2(\ddot{\theta} + \ddot{\phi})\alpha_{x\theta} = Q_k,$$

where the $\alpha_{x\theta}$ term is derived using the same method as that used in NHL, and the Q_k is given by Equation (11).

All three methods were processed using the symbolic computing software Maple to formulate the equation of motion for $\ddot{x}$. That equation was simplified to be written entirely in terms of $\dot{y}$ and $\dot{\theta}$, as defined in Equations (3a) and (5). Once all three methods produced identical equations of motion, the results were exported to MATLAB, and the built-in MATLAB numerical solver `ode45` was used to solve for the state x, y, θ, and $\dot{x}$. Using trigonometry, the displacement, velocity, and acceleration at positions along the length of the fish could be calculated. Simulations could be run to model position, velocity, and acceleration of any coordinate on the fish (angular and cartesian). Parameters, as defined in Table 1, could be defined according to prototype values and changed as needed for a given run. In simulations, ground perturbations were ignored (assuming a flat and level ground), and a Coulomb damping parameter was chosen to best match the experimental data.

Experimental Methods

As we developed our mathematical model of the landfish, we constructed a prototype for testing. Our experimental platform for implementing fish-like motion consisted of a custom-designed wheeled robot with an elongated chassis of two rigid bodies connected by a gear-driven joint. The fish's total body measured 0.59 m in length, 0.038 m in width, and 0.060 m in height, with a total weight of 3.813 kg. The total coefficient of drag was estimated to be 0.0042 $\frac{\text{kg}}{\text{m}}$ by modeling the prototype as a plate with a rectangular frontal area.

Our biomimetic design was inspired by carangiform swimming observed in species such as mackerel. This locomotion pattern is characterized by undulations primarily in the posterior half of the body, with amplitude increasing toward the caudal fin. As shown in Figure 2, we positioned the gear-driven joint at approximately $\frac{2}{3}$ of the landfish's total length, connecting the rigid anterior body to the flexible posterior section. This configuration allows the posterior section to generate

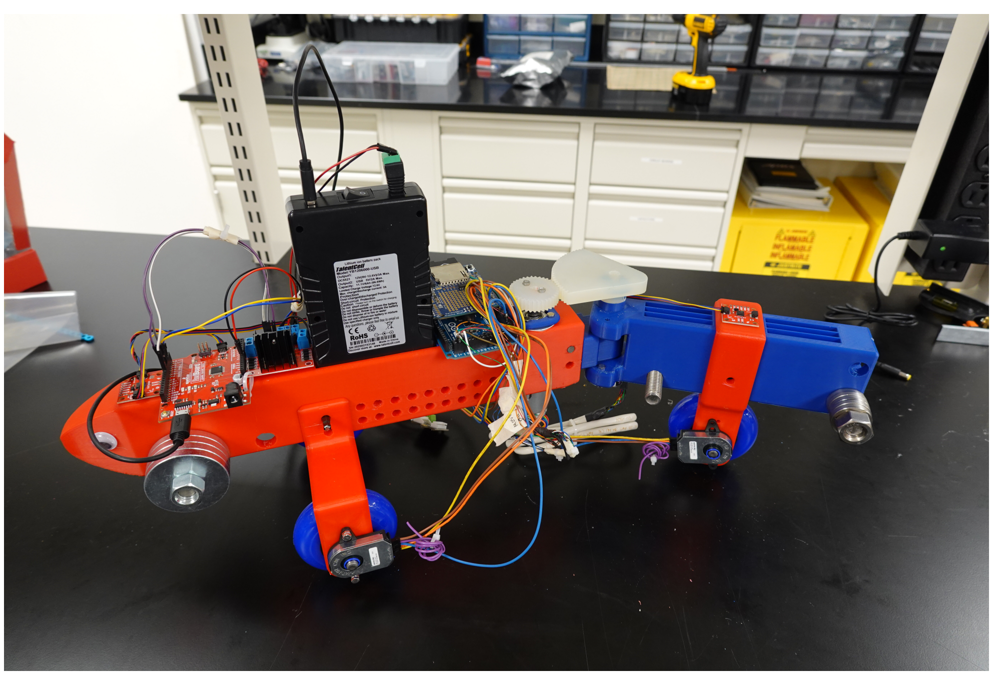

Fig. 2 Detailed view of the landfish prototype showing the two-body design connected by a gear-driven joint

the characteristic undulatory motion of a carangiform fish, with the gear mechanism enabling control of the tail's movement. A three-wheel configuration was chosen for stability, where the two front wheels together enforced the nonholonomic constraint on the head and the rear wheel enforced the nonholonomic constraint on the tail.

The chassis was primarily constructed of 3D-printed polylactic acid (PLA) with circular pin holes for wheel assembly placements. Figure 2 shows a detailed close-up of our prototype, highlighting the key mechanical components and joint configuration. $\frac{1}{2}''$ stainless steel threaded rods, washers of various sizes, and $\frac{1}{2}''$ nuts were added for two purposes: (1) to increase the overall weight of the robot and thereby enforce the nonholonomic constraints on the wheels through friction, preventing the wheels from slipping laterally during tail undulations, and (2) to ensure that the center of mass of each body was located over its respective wheel assembly to prevent tipping and simplify moment of inertia calculations.

For tracking wheel rotations, we integrated incremental encoders with each wheel assembly. To ensure a proper setup, we removed the two bearings from each of the three 70 mm polyurethane roller blade wheels and replaced them with printed PLA hubs. We then installed these bearings inside the 3D-printed wheel assemblies, such that the external surface of each bearing would remain stationary relative to the chassis, while the inner race spun with the axle. This configuration mirrored the encoder mounting, where each encoder body was rigidly attached to the outside of its respective wheel assembly housing. This design ensured that the encoder remained fixed to the non-rotating frame of reference while its sensing element detected the rotation of the spinning axle.

A sinusoidal control signal with adjustable amplitude and frequency parameters drove a 12 V gearmotor to create the undulating movements characteristic of fish locomotion. The gearmotor was housed within the head body's chassis and connected to a 2-gear system with a ratio of 35:95. The input gear was mounted on the motor shaft and the output gear was rigidly connected to the tail section. A long dowel pin ran through the output gear, the tail body, and the joint that connected the head and tail sections, serving as the axis of rotation between the two body segments. An absolute encoder was attached to the bottom of this pin to provide precise angular position feedback of the joint.

The electrical setup was implemented in two interconnected subsystems. The first subsystem consisted of a SparkFun RedBoard microcontroller connected to a motor driver that controlled the gearmotor. This drive system was responsible for generating the fish-like oscillatory motion, with the RedBoard processing the position feedback from the motor's built-in encoder and outputting the appropriate control signals to the motor driver. The second subsystem featured an Arduino Mega as the central controller, equipped with an Adalogger shield for data recording capabilities. This main board interfaced with four separate encoders: three incremental encoders attached to each wheel and one absolute encoder on the joint measuring ϕ. Additionally, two 9-axis inertial measurement units (IMUs) were integrated into this subsystem to capture motion dynamics on each body. The Arduino Mega coordinated the collection of sensor data from all these components, processed the information, and stored it on an SD card in the Adalogger for later analysis. Both the drive subsystem and the data acquisition subsystem were powered by a 12 V battery.

The data we collected primarily served to enable a comparison between our simulation and experimental results. From the comparison, we aimed to inform calibration of model parameters and validate simulation results. We performed standard calibration procedures for our rotational encoders and IMU sensors (linear acceleration and gyroscopic measurements). For our parameter study, we held multiple trials where we varied both amplitude and frequency of the prototype's tail motion and collected all relevant data from our sensors so that we could reconstruct and analyze its motion to compare with our simulations run with similar frequency and amplitude parameters. At the bottom of our range, we tested at a tail frequency of 1 Hz and a tail amplitude of 15 deg. At the top of our range, which was constrained by the limits of our prototype, we tested at 2 Hz and 35 deg. We tested in increments of 0.5 Hz and 5 deg ($\frac{\pi}{36}$ rad), totaling 15 trials in our parameter study.

To prepare our testing space for our experiment, we marked off a region of relatively flat hallway with a length of 20 m. Between trials, we updated and uploaded the motor control code to test a new set of parameters, and saved the data file from the previous trial. We then returned the prototype to the starting position (marked with tape) and aligned the front wheels so that they pointed down the hallway. Before the start of every run, the motor controller calibration routine rotated the tail to its limits in both directions in order to calculate and return to the center. This process occurred after the prototype was placed at the starting line. Thus the motion typically pushed the prototype off of the starting line and resulted in varied initial trajectory for each run. We determined that a trial was over if any of the following criteria were met: the prototype successfully reached the opposite end of the testing space, the prototype stopped moving forward, the prototype began veering severely, or if it was on a collision course with something else in the testing space.

Data Processing

After collecting encoder, accelerometer, and gyroscopic data from our experiments, we developed a standard data processing workflow that consisted of two main steps: cleaning and analysis. The cleaning step involved extracting data from the collected files followed by applying simple calibration tests to align our axes. We then spatially aligned accelerometer and gyroscopic data, positively aligned encoder data, and zeroed joint encoder data at the center of rotation. During this processing, we observed that our accelerometers were recording non-zero acceleration values in all three axes even when the system was completely at rest, making this data unreliable. Because of this, we decided to extract our position history solely from the encoder data. With the encoder data, we employed odometry to compute the position of each body at each time step. The cleaning process consisted of windowing the raw data to look at time periods we believed to be close to steady-state. To eliminate any influence on the data caused be veering and different starting trajectories, we then detrended it by calculating a linear fit and removing the slope of that line to center the data around $y = 0$ to spatially align it more closely with our model. To reduce noise acquired through numerical processes, we cleaned our simulation results in a similar manner.

Results & Discussion

In this section, we analyze and compare the results of our mathematical model predictions with experimental data from the wheeled landfish prototype, examining both motion patterns and performance across varying tail oscillation parameters.

Numerical solutions of the model with parameter values that matched the prototype's parameters demonstrated carangiform-like oscillatory locomotion which reached a steady-state mean velocity. Figure 3 shows an example of such motion from rest. The red and blue curves indicate the trajectory of the head and tail, respectively, where the initial position and orientation of the head was $(x, y, \theta) = (0, 0, 0)$. The sinusoidal path demonstrates how oscillatory tail motion generates forward propulsion while producing the characteristic undulatory motion observed in carangiform swimming.

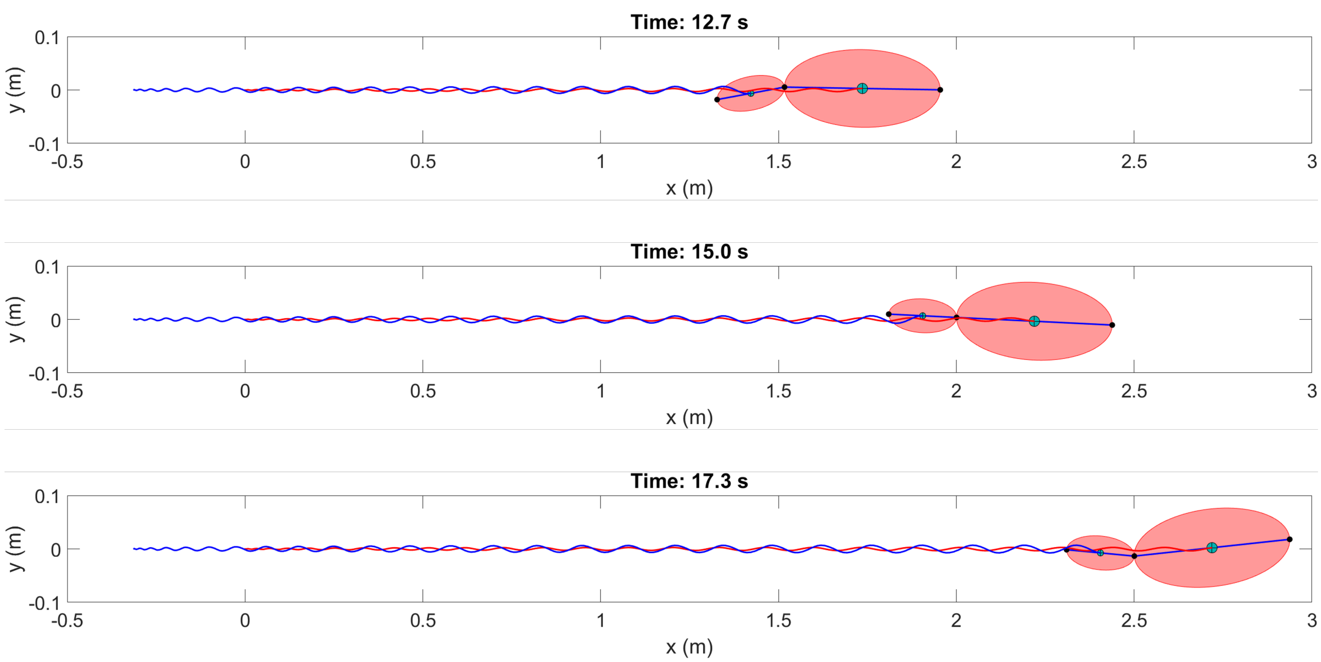

Fig. 3 The figure illustrates the trajectory of the landfish over time, with the head (blue) and tail (red) segments represented at sequential time steps

Our calibration trials successfully aligned coordinate systems and validated sensor functionality. Through linear and gyroscopic tests, we determined the orientation of the IMU axes and performed coordinate transformations. Encoder calibrations also confirmed the manufacturer's specification of 20,480 counts per revolution. However, from our stationary test, we observed unreliable readings from the IMUs. Over a 10-second period where both the IMUs and prototype remained still, the acceleration data indicated that the prototype experienced significant acceleration in all directions, which was deemed unreasonable. Therefore, we relied completely on the encoder data for information about the displacement, velocity, and acceleration. Initial experimental trials produced trajectory data that exhibited both the desired fish-like locomotion patterns and some expected deviations due to environmental factors. Figure 4 presents the unprocessed overhead trajectory of the wheeled landfish prototype over one trial. These paths demonstrate the characteristic undulating motion pattern but also show the veering tendency that necessitated the detrending step of our data cleaning process for comparative analysis.

The varying path curvatures observed in these trials reflect the sensitivity of the real system to slight asymmetries in the mechanical setup and ground irregularities.

After implementing the cleaning process of windowing and detrending, we were able to more directly compare the results of our experiment with our model. Figure 5 shows sample detrended trajectories over an 8 m path. The red and blue curves

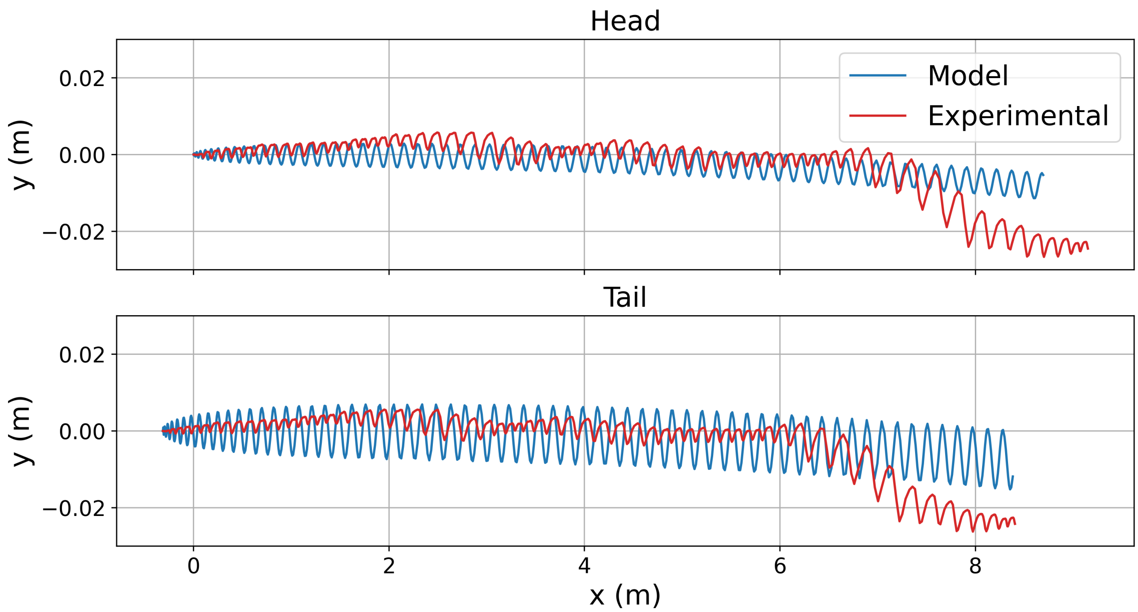

Fig. 4 The two plots compare the simulated/commanded (blue) and experimental/realized (red) overhead trajectories for each body over a 45-second interval with identical commanded tail oscillation parameters (25 deg amplitude, 1.5 Hz frequency)

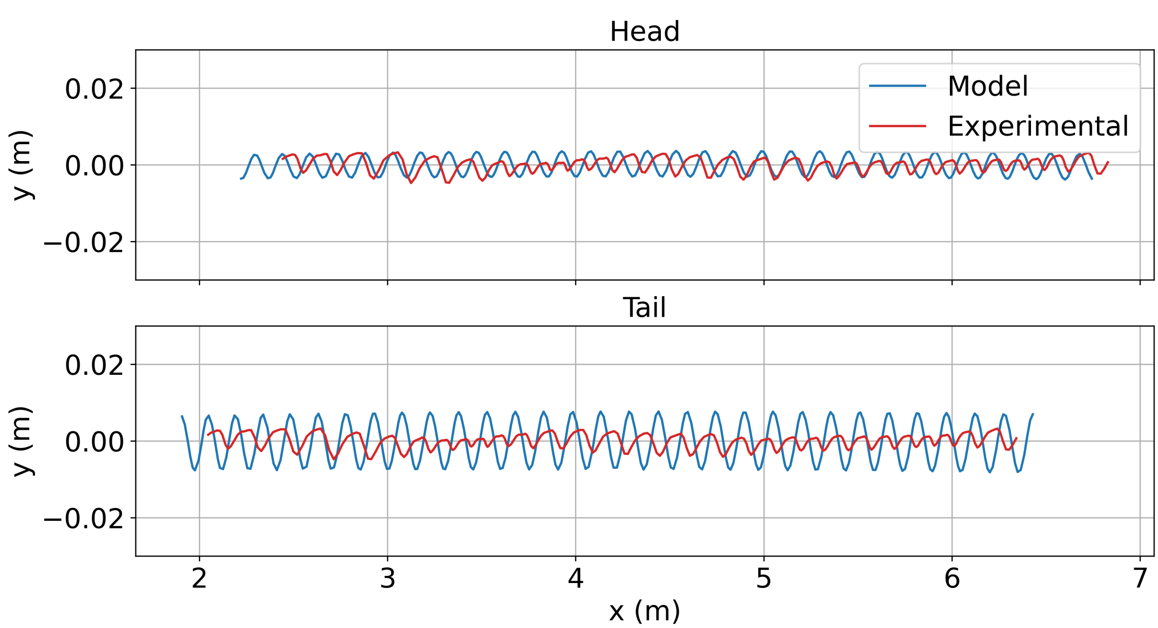

Fig. 5 These plots extend the analysis presented in Figure 4, with data windowed to the 15-35 second interval to exclude transient responses and trajectory deviations likely resulting from surface irregularities

show the experimental trajectory and simulated trajectory, respectively, where simulation parameters were chosen to match the experiment. Our results are encouraging; qualitatively, we see that the experimental data and simulation results produce similar overhead motion plots.

In Figure 6, we compare data from the absolute encoder placed on the joint and the imposed angle ϕ from our most successful run. We see that the frequency was imposed very well, however the amplitude appears to differ from that of the simulation. The experimental data shows a slight shift upward, which likely results from the fact that the friction in the gearmotor was observed to be asymmetrical, causing suspected controller saturation at high ϕ amplitude and frequency. Because of this, instead of producing a smooth sinusoidal curve, the motor oscillated with flattened troughs. At the peaks, the motor appeared to switch direction as desired. However, at the troughs, when the motor switched to rotate in the opposite direction, it appears to struggle (see Figure 6). We hypothesize that this could be one of the causes of the veering we observed in the prototype's overhead motion. These results show that the angle of rotation of the tail, ϕ, is not imposed as a perfect sine wave.

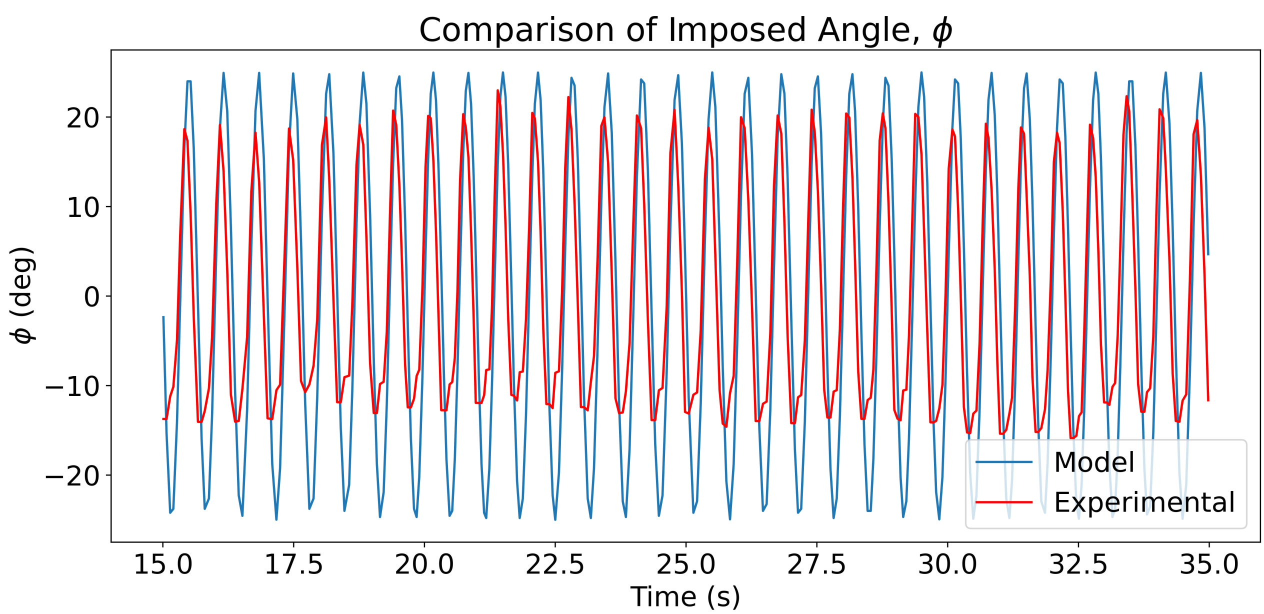

Fig. 6 The plot presents an alignment of simulated/commanded (blue) and experimental/realized (red) imposed tail angles, ϕ, throughout a trial period of 20 seconds with identical commanded tail oscillation parameters (25 deg amplitude, 1.5 Hz frequency)

To understand how changes in tail oscillation parameters affect locomotion, we conducted a parameter study on the mathematical model, which was bounded by the capabilities of our prototype according to the physical limits of the motor. Figure 7(a) shows how the simulation's horizontal steady-state velocity varies with the frequency and amplitude of the imposed tail angle, ϕ. The results from this study confirm our expectations: steady-state velocity increases with both the magnitude and frequency of tail oscillations, with the highest velocities occurring at maximum frequency and amplitude values within our tested range.

The experimental parameter study, shown in Figure 7(b), reveals a similar trend to our model predictions but with notable differences. Due to some of the difficulties with the experimental setup, this trend is only preserved for some ranges, notably where the angle between the head and the tail ϕ is imposed. This suggests the imposition of ϕ is essential to accurate prediction of motion and when ϕ is not accurately imposed there is a dramatic decrease in performance. In general, we found that our prototype behaved much more erratically than the model for several reasons, including ground perturbations in the test environment, asymmetric gearmotor performance in the prototype, and imperfect estimations of friction and drag. These are all sources of experimental uncertainty and potential causes of disagreement with the idealized simulation results.

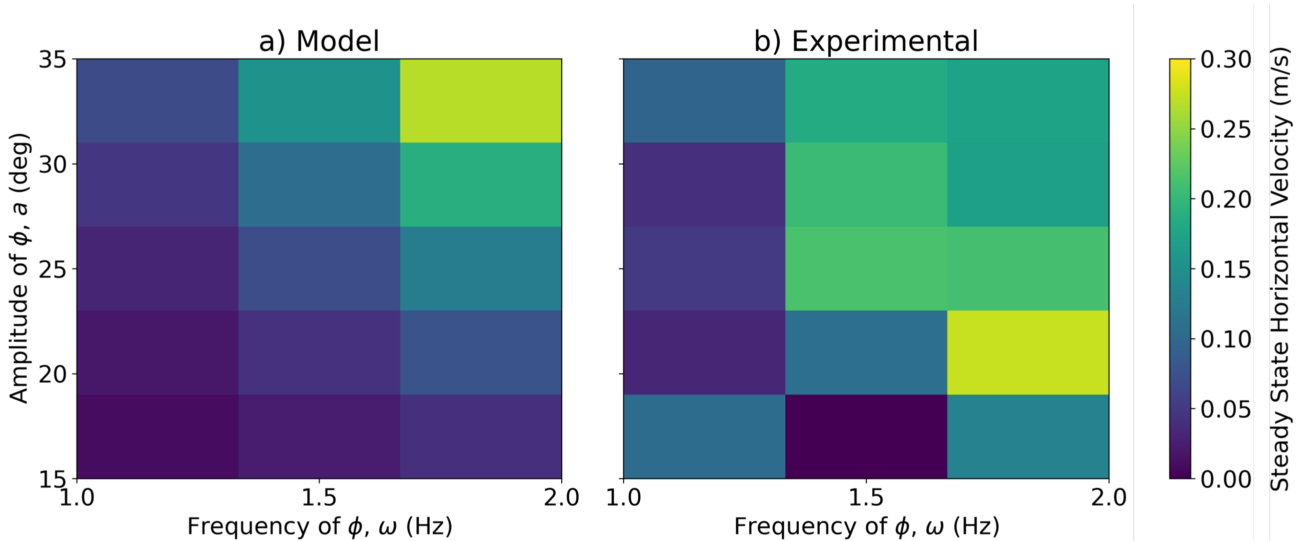

Fig. 7 Plots **a**) and **b**) detail the results of our simulated and experimental parameter studied, respectively. Both plots examine steady-state horizontal velocity as a function of the commanded frequency (x-axis) and amplitude (y-axis) of the imposed tail angle, ϕ. Each box corresponds to a trial at a particular ϕ frequency and amplitude and the color corresponds to the steady-state velocity found in each trial. The parameter space is bounded by our chosen experimental range of values

Conclusion

This study produced a reduced-order model of fish-inspired locomotion on land using nonholonomic constraints. By developing a landfish robot with a two-body system connected by a gear-driven joint, we demonstrated how oscillatory tail motion can generate forward propulsion on a wheeled platform through principles similar to carangiform swimming, without the added complexities of fluid dynamics. This work establishes a simplified framework that bridges biological principles with engineering implementation to rapidly design and optimize biomimetic robotic systems without exhaustive computational resources.

Our mathematical model, which employed three distinct methods (Lagrange multipliers, nonholonomic Lagrange, and the principle of virtual power) to derive the equations of motion, generated identical results that matched our expectations of the system's behavior. The model also predicted a relationship between tail oscillation parameters (frequency and amplitude) and the resulting locomotion patterns, showing that higher frequencies and amplitudes generally produced greater forward velocities within the operational limits of our prototype.

While the prototype successfully demonstrated fish-like propulsion in some runs, several challenges were encountered, which produced significant uncertainty in the experimental results. Ground irregularities prevented achieving true steady-state motion observed in simulations and caused the robot to veer during extended trials, highlighting both the sensitivity of nonholonomic systems to initial conditions and the limitations of our model's perfectly flat surface assumption, which is difficult to recreate in real-world testing environments. The robot's discrete segments further limited our ability to replicate the continuous and smooth undulation of fish locomotion.

The prototype could improve from future developments, such as a flexible body as well as smoother power transmission between bodies. For practical applications beyond laboratory settings, future designs would likely require robust and adaptive control systems for autonomous operation. Additionally, where our design positions centers of mass above wheel assemblies to simplify our model, investigation into varied mass distributions along the body would yield valuable insights into stability optimization, energy efficiency, and expanded maneuverability capabilities that could significantly enhance real-world performance in varied experimental conditions. Future work may address these limitations through the integration of additional articulated segments, improved surface interaction dynamics, enhanced control strategies for straight-line stability, and examination of varying surface conditions on operational performance. Along with these prototype modifications, the mathematical model would undergo equivalent changes. These would include new system-defining equations as bodies are added, an in depth parameter study to determine more accurate loss coefficients, a nonzero rotational stiffness coefficient of the head to ensure head oscillation about $y = 0$ and minimize veering, and introducing a third dimension to account for ground perturbations. With these changes, we hope the model and prototype will produce results that match even more accurately. Because of time constraints, we were not able to perform very in-depth or rigorous comparisons. Therefore, employing other analysis approaches that produce quantitative insights as well as qualitative would be beneficial. For example, beyond comparing overhead motion and ϕ profiles, proper and complex orthogonal decomposition could provide further insight into the motion of the landfish [23, 24].

Acknowledgments This research was funded by Los Alamos National Laboratory (LANL) through the Engineering Institute's Los Alamos Dynamics Summer School. The Engineering Institute is a research and education collaboration between LANL and the University of California San Diego's Jacobs School of Engineering. This collaboration seeks to promote multidisciplinary engineering research that develops and integrates advanced predictive modeling, novel sensing systems, and new developments in information technology to address LANL mission-relevant problems. This project was born out of work supported by the National Science Foundation (award number 2015194) at Michigan State University, which provided additional technical assistance and mentorship throughout the duration of this study.

References

1. J. Ardister and B. F. Feeny. "Modeling of Undulatory Swimming Motion Using Velocity Constraints". In: *Society for Integrative and Computational Biology*. SCIB+ Virtual. Presentation number 280. 2023.
2. International Union for Conservation of Nature. *Table 1a: Number of species evaluated in relation to the overall number of described species, and numbers of threatened species by major groups of organisms*. 2025. URL: https://nc.iucnredlist.org/redlist/content/attachment_files/2025-1_RL_Table_1a.pdf.
3. Xiaobo Tan, Michael Carpenter, John Thon, and Freddie Alequin-Ramos. "Analytical modeling and experimental studies of robotic fish turning". In: (2010), pp. 102–108. DOI: 10.1109/ROBOT.2010.5509488.
4. Robert L. McMasters, Casey P. Grey, John M. Sollock, Ranjan Mukherjee, Andre Benard, and Alejandro R. Diaz. "Comparing the mathematical models of Lighthill to the performance of a biomimetic fish". In: *Bioinspiration & Biomimetics* 3.1 (Feb. 2008), p. 016002. DOI: 10.1088/1748-3182/3/1/016002. URL: https://dx.doi.org/10.1088/1748-3182/3/1/016002.
5. Robert K. Katzschmann, Joseph DelPreto, Robert MacCurdy, and Daniela Rus. "Exploration of underwater life with an acoustically controlled soft robotic fish". In: *Science Robotics* 3.16 (2018), eaar3449. DOI: 10.1126/scirobotics.aar3449. URL: https://www.science.org/doi/abs/10.1126/scirobotics.aar3449.
6. Zihang Gao, Qing Shi, Toshio Fukuda, Chang Li, and Qiang Huang. "An overview of biomimetic robots with animal behaviors". In: *Neurocomputing* 332 (2019), pp. 339–350.
7. C. C. Lindsey. "1 - Form, Function, and Locomotory Habits in Fish". In: *Locomotion*. Ed. by W. S. Hoar and D. J. Randall. Vol. 7. Fish Physiology. Academic Press, 1978, pp. 1–100. DOI: https://doi.org/10.1016/S1546-5098(08)60163-6. URL: https://www.sciencedirect.com/science/article/pii/S1546509808601636.
8. Paul W. Webb. "3 - Hydrodynamics: Nonscombroid Fish". In: *Locomotion*. Ed. by W. S. Hoar and D. J. Randall. Vol. 7. Fish Physiology. Academic Press, 1978, pp. 189–237. DOI: https://doi.org/10.1016/S1546-5098(08)60165-X. URL: https://www.sciencedirect.com/science/article/pii/S154650980860165X.
9. J. J. Videler. *Fish Swimming*. Champman and Hall, London, 1993.
10. Michael Sfakiotakis, David M. Lane, and J. Bruce C. Davies. "Review of fish swimming modes for aquatic locomotion". In: *IEEE Journal of Oceanic Engineering* 24.2 (2002), pp. 237–252.
11. Iman Borazjani and Fotis Sotiropoulos. "Numerical investigation of the hydrodynamics of carangiform swimming in the transitional and inertial flow regimes". In: *Journal of Experimental Biology* 211.10 (May 2008), pp. 1541–1558. ISSN: 0022-0949. DOI: 10.1242/jeb.015644. URL: https://doi.org/10.1242/jeb.015644.
12. Afzal Suleman and Curran Crawford. "Design and testing of a biomimetic tuna using shape memory alloy induced propulsion". In: *Computers & Structures* 86.3-5 (2008), pp. 491–499.
13. Baofeng Liao, Zheng Li, and Ruxu Du. "Robot fish with a novel biomimetic wire-driven flapping propulsor". In: *Advanced Robotics* 28.5 (2014), pp. 339–349.
14. Kin Huat Low, Chee Wee Chong, and Chunlin Zhou. "Performance study of a fish robot propelled by a flexible caudal fin". In: *2010 IEEE International Conference on Robotics and Automation*. IEEE. 2010, pp. 90–95.
15. Jennie Cochran, Eva Kanso, Scott D. Kelly, Hailong Xiong, and Miroslav Krstic. "Source Seeking for Two Nonholonomic Models of Fish Locomotion". In: *IEEE Transactions on Robotics* 25.5 (2009), pp. 1166–1176. DOI: 10.1109/TRO.2009.2026500.
16. Michael J. Fairchild, Peter M. Hassing, Scott David Kelly, Parthesh Pujari, and Phanindra Tallapragada. "Single-Input Planar Navigation via Proportional Heading Control Exploiting Nonholonomic Mechanics or Vortex Shedding". In: *ASME 2011 Dynamic Systems and Control Conference and Bath/ASME Symposium on Fluid Power and Motion Control*. Vol. 1. Dynamic Systems and Control Conference. Oct. 2011, pp. 345–352. DOI: 10.1115/DSCC2011-6191. URL: https://doi.org/10.1115/DSCC2011-6191.
17. Beau Pollard, Vitaliy Fedonyuk, and Phanindra Tallapragada. "Swimming on limit cycles with nonholonomic constraints". In: *Nonlinear Dynamics 97* (2019), pp. 2453–2468.
18. J. Ardister and B. F. Feeny. "Modeling and Analysis of a Constrained Two-rigid-body System Using Nonholonomic Lagrange Equations". In: *International Design Engineering Technical Conferences, 34th Conference in Vibration and Noise*. IDETC2022-97866. St. Louis, MO, USA, 2022.
19. J. Ardister and B. F. Feeny. "Modeling of a Two-rigid-body Land-fish Using Nonholonomic Lagrange Equations". In: *International Mechanical Engineering Congress and Exposition*. IMECE2022-99574. Columbus, OH, USA, 2022.
20. T. Dear, S. D. Kelly, M. Travers, and H. Choset. "Mechanics and Control of a Terrestrial Vehicle Exploiting a Nonholonomic Constraint for Fishlike Locomotion". In: *ASME 2013 Dynamic Systems and Control Conference*. Vol. 2. ASME. 2013. DOI: 10.1115/DSCC2013-3941.

21. B. F. Feeny. "D'Alembert's Principle and the Equations of Nonholonomic Systems". In: *ASME International Mechanical Engineering Congress and Exposition*. IMECE2006/VIB-14533. 2006.
22. F. C. Moon. *Applied Dynamics, With Applications to Multibody and Mechatronic Systems*. Wiley-VCH Verlag GambH&Co. KGaA, Weinheim, 2008.
23. B. F. Feeny. "A Complex Orthogonal Decomposition for Wave Motion Analysis". In: *Journal of Sound and Vibration* 310.1 (2008), pp. 77–90. ISSN: 0022-460X. DOI: https://doi.org/10.1016/j.jsv.2007.07.047.
24. B. F. Feeny and A. K. Feeny. "Complex Modal Analysis of the Swimming Motion of a Whiting". In: *Journal of Vibration and Acoustics* 135.2 (Feb. 2013), p. 021004. ISSN: 1048-9002. DOI: 10.1115/1.4023056. URL: https://doi.org/10.1115/1.4023056.